University of Texas at Tyler
Scholar Works at UT Tyler

Mechanical Engineering Faculty Publications and Presentations | Mechanical Engineering

Spring 1-19-2023

Static and Dynamic Analysis of a Bistable Frequency Up-Converter Piezoelectric Energy Harvester

Mohammad Atmeh
University of Texas at Tyler, MAtmeh@patriots.uttyler.edu

Alwathiqbellah Ibrahim
University of Texas at Tyler, aibrahim@uttyler.edu

Abdallah Ramini

Follow this and additional works at: https://scholarworks.uttyler.edu/me_fac

 Part of the Mechanical Engineering Commons

Recommended Citation

Atmeh, Mohammad; Ibrahim, Alwathiqbellah; and Ramini, Abdallah, "Static and Dynamic Analysis of a Bistable Frequency Up-Converter Piezoelectric Energy Harvester" (2023). *Mechanical Engineering Faculty Publications and Presentations.* Paper 28.
http://hdl.handle.net/10950/4437

This Article is brought to you for free and open access by the Mechanical Engineering at Scholar Works at UT Tyler. It has been accepted for inclusion in Mechanical Engineering Faculty Publications and Presentations by an authorized administrator of Scholar Works at UT Tyler. For more information, please contact tgullings@uttyler.edu.

micromachines

MDPI

Article

Static and Dynamic Analysis of a Bistable Frequency Up-Converter Piezoelectric Energy Harvester

Mohammad Atmeh [1], Alwathiqbellah Ibrahim [1,*] and Abdallah Ramini [2]

[1] Department of Mechanical Engineering, The University of Texas at Tyler, 3900 University Blvd., Tyler, TX 75799, USA
[2] Shock and Vibration Lab-IBM Corporation, 2455 South RD, Poughkeepsie, NY 12601, USA
* Correspondence: aibrahim@uttyler.edu

Abstract: Using energy harvesting to convert ambient vibrations efficiently to electrical energy has become a worthy concept in recent years. Nevertheless, the low frequencies of the ambient vibrations cannot be effectively converted to power using traditional harvesters. Therefore, a frequency up-conversion harvester is presented to convert the low-frequency vibrations to high-frequency vibrations utilizing magnetic coupling. The presented harvester consists of a low-frequency beam (LFB) and a high-frequency beam (HFB) with identical tip magnets facing each other at the same polarity. The HFB, fully covered by a piezoelectric strip, is utilized for voltage generation. The dynamic behavior of the system and the corresponding generated voltage signal has been investigated by modeling the system as a two-degrees-of-freedom (2DOF) lumped-parameter model. A threshold distance of 15 mm that divides the system into a monostable regime with a weak magnetic coupling and a bistable regime with a strong magnetic coupling was revealed in the static analysis of the system. Hardening and softening behaviors were reported at the low frequency range for the mono and bistable regimes, respectively. In addition, a combined nonlinear hardening and softening behavior was captured for low frequencies at the threshold distance. Furthermore, a 100% increment was achieved in the generated voltage at the threshold compared to the monostable regime, and the maximum generated voltage was found to be in the bistable regime. The simulated results were validated experimentally. Moreover, the effect of the external resistance was investigated, and a 2 MΩ resistance was found to be optimal for maximizing the generated power. It was found that frequency up-converting based on magnetic nonlinearity can effectively scavenge energy from low-frequency external vibrations.

Keywords: piezoelectric; energy harvesting; up-conversion; bistable; magnet

check for updates

Citation: Atmeh, M.; Ramini, A.; Ibrahim, A. Static and Dynamic Analysis of a Bistable Frequency Up-Converter Piezoelectric Energy Harvester. *Micromachines* **2023**, *14*, 261. https://doi.org/10.3390/mi14020261

Academic Editor: Wei Li

Received: 12 December 2022
Revised: 15 January 2023
Accepted: 15 January 2023
Published: 19 January 2023

Copyright: © 2023 by the authors. Licensee MDPI, Basel, Switzerland. This article is an open access article distributed under the terms and conditions of the Creative Commons Attribution (CC BY) license (https://creativecommons.org/licenses/by/4.0/).

1. Introduction

The continuous development in technology has recently led to improved power generation resources by transferring them from conventional to non-conventional. Conventional power resources, such as batteries, are limited due to their short lifespans and the ability to store power, so they require charging overtime. Therefore, harvesting energy from the ambient is an attractive concept that could remove the need for batteries and their limitations [1]. Mechanical vibrations are considered one of the most wasted energies that are abundant around us in the environment. They are present during our daily activities, such as driving and walking [2–4]. Consequently, research is constantly attempting to convert those mechanical vibrations to electrical energy to power wireless sensors and electronics that work in the micro-to-milliwatts range [5].

Nature is rich with mechanical vibrations that are abundant at low-frequency ranges [6]. Thus, benefits from ambient energy by harvesting those vibrations will provide a non-conventional power resource [7]. Different mechanisms are used to convert mechanical vibrations into electrical power. Electromagnetic [8], triboelectric [9,10], and piezoelectric [11] mechanisms are the most common. Among all these mechanisms, piezoelectric

energy harvesters have the ability to work at a low power level and resist environmental conditions; therefore, they have been utilized in several environmental applications, such as being implanted inside the human body [12,13], civil infrastructure [14,15], and aerospace systems [16–20]. However, some drawbacks include the high resonance frequency which is away from the ambient ranges [2,21] and the narrow bandwidth [22]. Therefore, several techniques have been utilized to overcome these drawbacks, such as the nonlinearity contribution [23–30], circuit management [31], the double pendulum system [32], frequency-tunable oscillators [33–35], and frequency up-conversion [36]. Nonlinearity has contributed to expanding the bandwidth of the output power by influencing the mechanical [37,38], impact [39], and magnetic [30,40,41] effects.

To increase the efficiency of harvesting energy from low-frequency vibrations, the frequency up-converter has been investigated lately [36,42–50]. Basically, the approach of the frequency up-converter is that the low-frequency sources induce high-frequency oscillations [51]. This inducing can be obtained either by the impact [52] or by plucking [53]. An impact between low-frequency and high-frequency beams will change the ambient vibrations into high-frequency vibrations [42,54]. This would improve the low-frequency vibration harvesters, filling the gap between the low-frequency excitation and high-frequency response [55,56]. In addition, to increase the reliability and eliminate the issues of mechanical contact, magnetic coupling has been investigated as a non-mechanical contact method [36,45,57,58]. The low-frequency motions of animals were up-converted through a self-powered magnetoacoustic into high-frequency acoustic signals [59]. On the other hand, an electromagnetic frequency up-converter was used with magnets and coils on top of a resonator beam to generate power [58].

The magnetic nonlinear behaviors of softening and hardening can be achieved by controlling the separation distance between two magnets facing each other at the same polarity [30]. Broadening the bandwidth has been investigated by using microscale [60–62] and macroscale [21] monostable energy harvesters. Additionally, bistability was used to increase the frequency bandwidth and the magnitude of the output power [22,63–69]. Experimental results show that the maximum power is produced at the transition region between the monostable and the bistable regime [30,70,71]. Additionally, external load resistance was optimized in a magnetically coupled, two-degrees-of-freedom, bistable energy harvester to maximize the output power [72]. In addition, the effect of spring stiffness at low excitation frequencies under Gaussian white noise excitation causes a significant improvement in the harvesting efficiency of bistable energy harvesters [73].

In this study, we propose a frequency up-conversion method to harvest low-frequency ambient vibrations utilizing piezoelectric material for voltage generation. The frequency up-converter couples two cantilever beams mechanically using two identical magnets to convert low-frequency vibrations to high-frequency oscillations. The two cantilever beams have identical tip magnets facing each other at the same polarity, which induces magnetic coupling between both beams' oscillations. The system of beams was modeled as a two-degree-of-freedom (2DOF) lumped-parameter model to investigate the dynamic behavior and generated voltage signal.

The remainder of this article begins with presenting the configuration of the device and the working mechanism of the frequency-up-converter energy harvester. The static response of each beam, the frequency variation and separation distance relation, and the voltage generation at different separation distance values are explored. Additionally, the simulation results from the theoretical model are validated experimentally.

2. Device Configuration and Principle of Operation

A 3D model and a 2D schematic for the system are shown in Figure 1a and Figure 1b, respectively. The system consists of two cantilever beams with identical masses attached to the beams' tips, as shown in Figure 1a. In Figure 1b, the beam is unimorph and fully covered by a piezoelectric strip to generate voltage, and it is made of aluminum for higher natural frequency and is called the high-frequency beam (HFB). On the left-hand side,

the beam is made of a polymer material for lower natural frequencies and it is called the low-frequency beam (LFB). The tip masses are two identical magnets facing each other at the same polarity to utilize the generated repulsive force to create a nonlinear mechanical coupling that will transfer the energy between both beams to create a frequency-up-converter energy harvester. L1 and L2 are the lengths of the LFB and HFB, respectively. The beams are separated horizontally by a distance d, and the piezoelectric strip is connected to an external resistor R. The beams are attached to a holder, and the whole setup is installed on an electrodynamic shaker, as shown in Figure 1a. The system was subjected to a base excitation level ($a(t)$) applied by the electrodynamic shaker.

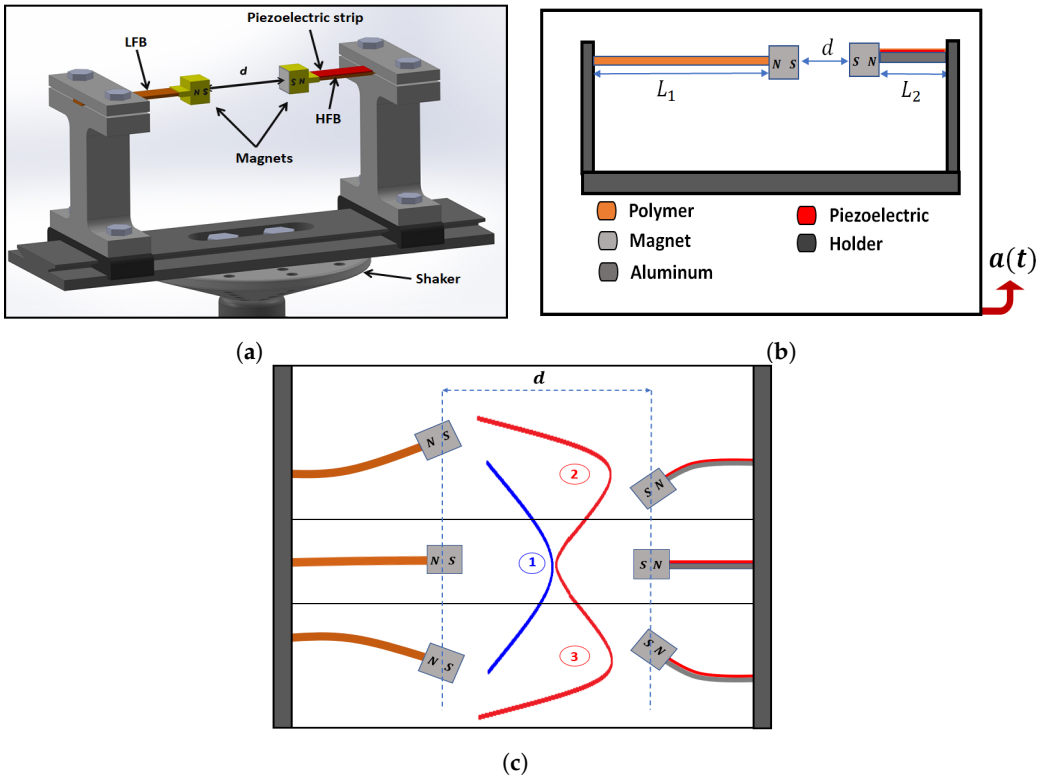

Figure 1. (**a**) A 3D model of the energy harvester system. (**b**) A 2D schematic of the energy harvester system. (**c**) The mono and bistable principles of operation under repulsive magnetic force.

When the separation distance, d, decreases, the repulsive magnetic force between the tip magnets will increase and induce a strong nonlinearity in the system that will transfer the potential energy of the resonator from a monostable phase (the resonator oscillates around a single equilibrium point) to a bistable phase (the resonator oscillates around two equilibrium points). When the separation distance increases, the magnetic force will be weak, and the system will oscillate in a monostable phase where each beam will oscillate around its horizontal axis around a single-well stable equilibrium point, as shown in Figure 1c, case 1. On the other hand, decreasing the separation distance will strengthen the magnetic force so each beam will oscillate around two stable points, either above or below the horizontal axis, as in cases 2 and 3 in Figure 1c, so two potential wells will be developed for each beam.

3. Theoretical Model

The shaker excites the frequency up-converter that consists of two cantilever beams with identical tip magnets facing each other at the same polarity. Both beams will oscillate, and the energy will be transferred from the low-frequency range to the high-frequency range due to the magnetic coupling between the tip magnets. This oscillation will develop the required stresses and strains to bend the beams to generate a voltage from the piezoelectric strip attached to the HFB, as shown in Figure 2a. The tip magnets will affect each other

by a repulsive magnetic force with the same magnitude because they are identical, and the produced forces can be analyzed as vertical and horizontal components; see Figure 2a. Based on its geometry, the frequency up-converter is modeled as a two-degrees-of-freedom (2DOF) lumped-parameter model subjected to harmonic base excitation, as shown in Figure 2b.

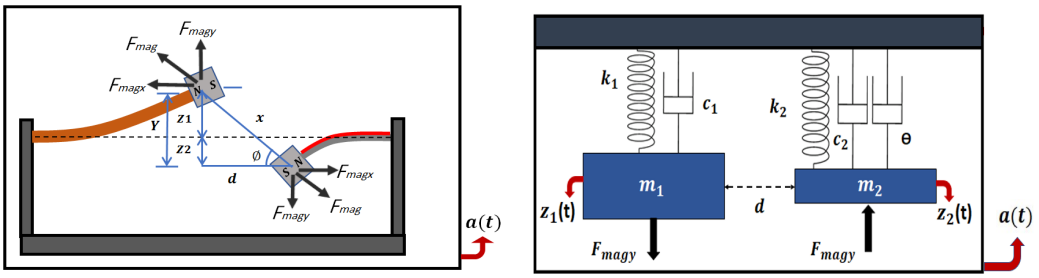

(**a**) (**b**)

Figure 2. (**a**) Magnetic interactions between LFB and HFB. (**b**) Two-degrees-of-freedom spring-mass-damper systems for the LFB and HFB.

From Figure 2b, the LFB and HFB are modeled as two-degrees-of-freedom (2DOF) spring-mass-damper systems. Accordingly, the governing equations that describe the system, including the coupling between the HFB and the piezoelectric strip, are as follows [72]:

$$\begin{aligned} &m_1\ddot{z_1}(t) + c_1\dot{z_1}(t) + k_1 z_1(t) + F_{magy} = m_1 a(t) \\ &m_2\ddot{z_2}(t) + c_2\dot{z_2}(t) + k_2 z_2(t) + \theta v(t) - F_{magy} = m_2 a(t) \\ &\dot{v}(t) - \chi\dot{z_2}(t) + \lambda v(t) = 0 \end{aligned} \tag{1}$$

where $a(t)$ is the harmonic base excitation ($a(t) = A\,cos(\Omega\,t)$), Ω is the excitation frequency, and A is the amplitude. $z_1(t)$ and $z_2(t)$ are the displacements of the LFB and the HFB, respectively. Additionally, m_1 and k_1 are the equivalent mass and the stiffness of the LFB, respectively, and m_2 and k_2 are the equivalent mass and the stiffness of the HFB, respectively. The damping coefficients for the LFB and HFB are c_1 and c_2, respectively. Additionally, $v(t)$ is the voltage generated from the piezoelectric layer, and $\lambda = 1/RC_p$, such that R is the resistance and C_p is the capacitance ($C_p = (\epsilon_{33} b_p L_p)/h_p$), where ϵ_{33} is the permittivity ($3250 \times 8.854 \times 10^{-12}$); b_p, L_p, and h_p are the piezoelectric layer's width, length, and thickness, respectively. Additionally, χ can be calculated as $\chi = \frac{\theta}{C_p}$, where θ is the coupling coefficient of the piezoelectric layer. Additionally, the fundamental natural frequencies of both beams can be calculated from the following formula:

$$f_i = \frac{1}{2\pi}\sqrt{\frac{k_i}{m_i}}\,,\ i = 1, 2. \tag{2}$$

where m_i and k_i are the equivalent mass and the stiffness of the beams, respectively. For the LFB, the stiffness can be calculated as ($k_1 = 3E_1 I_1 / L_1^3$) [74], and for the HFB, it can be calculated as ($k_2 = 3E_p I_{eq} / L_2^3$). The stiffness of the HFB represents the equivalent stiffness of the piezoelectric layer and the HFB beam. The HFB's equivalent mass consists of the piezoelectric layer mass (m_p) and the effective mass of the cantilever beam ($m_{heff} = 0.375 m_b$) [74], where m_b is the beam mass. E_p represents the modulus of elasticity of the piezoelectric strip. I_{eq} is the equivalent moment of inertia of the HFB and piezoelectric strip and can be calculated using Equation (3) [74].

$$I_{eq} = \frac{W_p t_p^3}{12} + (t_p W_p (t_h + \frac{t_p}{2}) - Y_n)^2 + \frac{n W_p t_h^3}{12} + t_h n W_p (\frac{t_h}{2} - Y_n)^2 \tag{3}$$

where Y_n is the location of the neutral axis of the HFB with the piezoelectric strip and can be calculated using Equation (4). Additionally, t_p and t_h are the thickness of the piezoelectric strip and the HFB, respectively. W_p represents the width of the piezoelectric strip, and n is the ratio of the modulus of elasticity of the HFB to the modulus of elasticity of the piezoelectric strip ($n = E_h/E_p$).

$$Y_n = \frac{(\frac{t_p}{2} + t_h)t_p + (\frac{t_h}{2})nt_h}{(t_p + t_h n)}. \tag{4}$$

By evaluating the neutral axis location, Y_n, the electro-mechanical coupling factor, θ, can be calculated as:

$$\theta = d_{31}\left(\frac{k_2 b_2 L_2 (L_2 + L_p) Y_n}{2I_{eq}}\right) \tag{5}$$

where d_{31} is the piezo strain constant. Additionally, b_2 is the width of the HFB and L_p is the length of the piezoelectric strip. The coupling magnetic force is a function of the separation distance (d) between the LFB and HFB beams, and it can create either a mono or bistable system as demonstrated in Figure 1c. This magnetic force can be calculated as [30]:

$$F_{mag} = \frac{F_R}{X^4} \tag{6}$$

where X is the distance between the centers of the two magnets ($X = \sqrt{d^2 + Y^2}$), and Y is the total vertical deflection between the two tip magnets given by $Y = z_1(t) + z_2(t)$. F_R is a function of the moments for magnetic dipoles (q_1 and q_2) and the permeability of the free space ($\epsilon = 4\pi \times 10^{-7}$ m kg/s^{2}A^2), and is given by $F_R = (3\epsilon q_1 q_2)/2\pi$. According to Figure 2a, the total magnetic force can be analyzed using the angle ϕ into a horizontal component F_{magx}, which is assumed to be equivalent to the longitudinal stiffness of the beams, and a vertical component (F_{magy}) in the transverse direction, which is responsible for the beams transverse deflections and is given by the following equation:

$$F_{magy} = \frac{F_R Y}{(d^2 + Y^2)^{5/2}} \tag{7}$$

4. Experimental Setup

The experimental setup used for testing the harvester is shown in Figure 3. The setup consists of the VR9500 control unit, amplifier, electrodynamic shaker, and energy harvesting structure. The control unit controls the amplitude and frequency of the base excitation applied by the electrodynamic shaker. The amplifier receives the signal from the control unit and then it sends it to the shaker. Once the shaker receives the signal from the amplifier, it starts shaking and acting as a base excitation for the harvester structure. The frequency response curves of the LFB and HFB beams are measured by accelerometers attached to the tip magnet of each beam. The accelerometers are connected to the VR9500 control unit and measure the beams' vibrations as a function of the excitation frequencies. Additionally, the voltage is generated by a piezoelectric strip attached to the HFB. When the beam oscillates, its deflection develops stress and strain on the piezoelectric strip, resulting in an alternative voltage signal being generated and recorded by the controller.

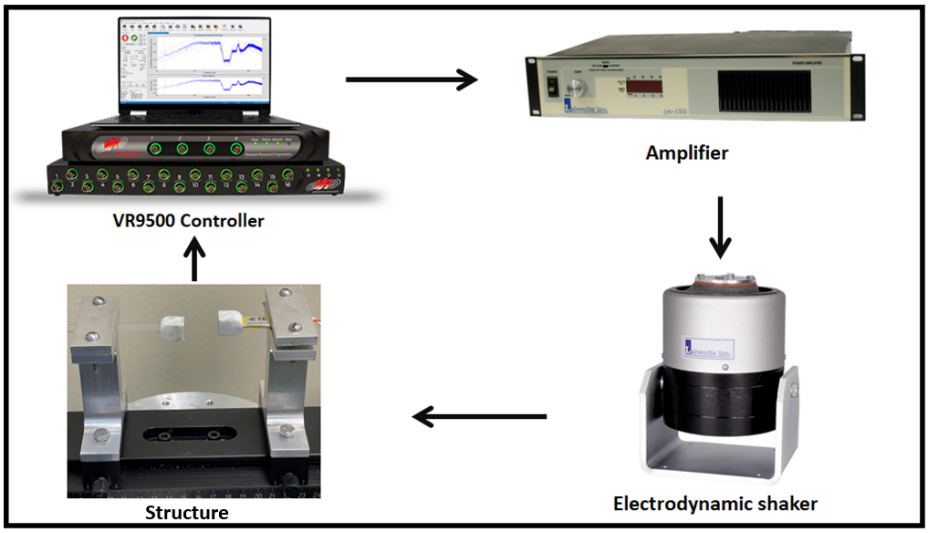

Figure 3. Experimental setup used to test the piezoelectric energy harvester frequency up-converter.

5. Results and Discussion

5.1. Static Analysis

By setting all the time-derivatives to zero in Equation (1), the static response of both beams, the LFB and HFB, under the effect of the magnetic coupling, can be calculated as follows:

$$\begin{aligned} k_1 z_{1s} + F_{magys} &= 0 \\ k_2 z_{2s} - F_{magys} &= 0 \end{aligned} \tag{8}$$

where z_{1s} and z_{1s} represent the static deflections of the LFB and HFB, respectively. F_{magys} is the static magnetic force in the vertical direction, and it is given by the following formula:

$$F_{magys} = \frac{F_R Y_s}{(Y_s^2 + d^2)^{5/2}} \tag{9}$$

where Y_s is the static deflection of both beams between the magnets' centers and is given by $Y_s = z_{1s} + z_{2s}$. Using the geometrical parameters listed in Table 1, the static solution for Equation (8) can be extracted. Figure 4a,b show the theoretical and experimental static response of the LFB and the theoretical static response of the HFB, respectively, with the variation in the horizontal distance between the two tip magnets. It is clearly shown that a critical threshold separation distance is $d_{th} = 15$ mm. This threshold distance divides the system into two main parts, a monostable region where $d > d_{th}$ and a bistable region where $d < d_{th}$. In the monostable region, the static profiles of both beams show single stable branches, where both beams oscillate around a single equilibrium point in the middle. In the bistable range, each static profile shows two upper and lower stable branches and one unstable branch in the middle. Each beam will oscillate between the two stable equilibrium points in the bistable range. Figure 4a shows good agreement between the theoretical and experimental results of the LFB. The experimental measurements of the LFB were taken by measuring the separation distance (d) between the centers of both tip magnets using a ruler. Once the LFB starts showing a significant deflection by moving towards the threshold and bistable regions, the vertical deflection of the LFB gets measured between the original horizontal axis of the beam and the new location of the tip magnet center. The HFB is a stiff beam with minimal deflections that may need an advanced measurement system, such as one using laser technology, to be captured experimentally. However, the match between the experimental and simulated results for the LFB indicates our model's ability to capture the correct static behavior for the HFB.

Table 1. Physical and geometrical parameters of the frequency up-converter piezoelectric energy harvester.

Parameters	Symbol	Value
LFB (length × width × thickness)	$L_1 \times b_1 \times h_1$	$(26 \times 10 \times 1)$ mm
LFB Young's modulus	E_1	2.344 Gpa
LFB Density	ρ_1	1220 kg/m^3
LFB Damping coefficient	c_1	0.0038 N s/m
HFB (length × width × thickness)	$L_2 \times b_2 \times h_2$	$(19 \times 10 \times 1.6)$ mm
HFB Young's modulus	E_2	69.0 Gpa
HFB Density	ρ_2	2700 kg/m^3
HFB Damping coefficient	c_2	0.38 N s/m
Piezoelectric (length × width × thickness)	$L_p \times b_p \times h_p$	$(19 \times 7 \times 0.02)$ mm
Piezoelectric Young's modulus	E_p	2450 Mpa
Piezoelectric Density	ρ_p	1780 kg/m^3
Resistance	R	200 kΩ
Magnets side length	L_m	8.0 mm
Magnetic moment	$q_1 = q_2$	0.5 A^2/m
Piezo Strain Constant	d_{31}	23×10^{-12}
Piezoelectric Laminate permittivity	ϵ_{33}	$3250 \times 8.854 \times 10^{-12}$

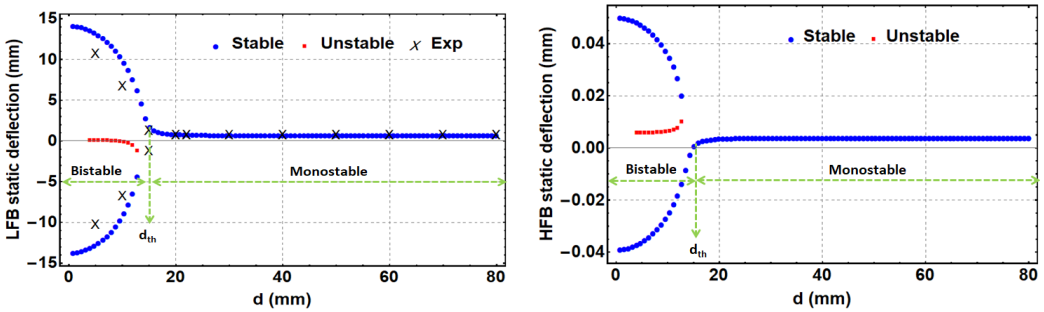

(**a**) (**b**)

Figure 4. The static response of the LFB and HFB versus the separation distance. (**a**) Experimental and theoretical static response of the LFB, (**b**) theoretical response of the HFB. Threshold value, d_{th}, found to be 15 mm.

5.2. Dynamic Analysis

5.2.1. Natural Frequencies

To solve for the natural frequencies of the system as a function of the separation distance, we assume the total deflection of the beams to be a function of the static and dynamic deflections as:

$$\begin{aligned} z_1(t) &= u_1 + z_{1s} \\ z_2(t) &= u_2 + z_{2s} \end{aligned} \tag{10}$$

where u_1 and u_2 are the dynamic deflections for the LFB and HFB, respectively. Accordingly, the total vertical deflection will be:

$$Y = Y_s + Y_u. \tag{11}$$

where Y_u is dynamic deflection and given by $Y_u = u_1 + u_2$. By substituting Equation (11) into Equation (9), the vertical magnetic force will be:

$$F_{magy} = \frac{F_R(Y_s + Y_u)}{(d^2 + (Y_s + Y_u)^2)^{5/2}} \tag{12}$$

Substituting Equations (2)–(12) into Equation (1) will result in the following governing equation:

$$\begin{aligned} &m_1\ddot{u_1}(t) + c_1\dot{u_1}(t) + k_1(u_1 + z_{1s}) + F_{magy} = m_1a(t) \\ &m_2\ddot{u_2}(t) + c_2\dot{u_2}(t) + k_2(u_2 + z_{2s}) + \theta v(t) - F_{magy} = m_2a(t) \\ &\dot{v}(t) - \chi\dot{u_2}(t) + \lambda v(t) = 0 \end{aligned} \tag{13}$$

To cancel the static effect according to the static Equation (Equation (10)), and to avoid the complications of the magnetic formula in getting the numerical solution, the magnetic force, F_{magy}, was expanded using Taylor's series around zero dynamic deflection ($Y_u = 0$) for up to nine terms. Accordingly, the magnetic force will be:

$$\begin{aligned} F_{magy} &= \frac{F_R Y_s}{(d^2 + Y_s^2)^{5/2}} + \sum_{i=1}^{9} \alpha_i Y_u^i(t), \qquad i = 1, 2, \ldots 9 \\ &= F_{magys} + F_{magyu} \end{aligned} \tag{14}$$

where α_i are the coefficients of Taylor's series expansion of the dynamic magnetic force, and they are listed in Appendix A. F_{magys} and F_{magyu} represent the static and dynamic magnetic force, respectively. When Equation (14) is substituted into Equation (13), the static terms will cancel each other since they are equal to zero, as shown in Equation (8); therefore, the governing equations of the system will be:

$$\begin{aligned} &m_1\ddot{u_1}(t) + c_1\dot{u_1}(t) + k_1u_1 + F_{magyu} = m_1a(t) \\ &m_2\ddot{u_2}(t) + c_2\dot{u_2}(t) + k_2u_2 + \theta v(t) - F_{magyu} = m_2a(t) \\ &\dot{v}(t) - \chi\dot{u_2}(t) + \lambda v(t) = 0 \end{aligned} \tag{15}$$

Now, by substituting the dynamic magnetic force of Equation (14) in Equation (15), and using $Y_u = u_1 + u_2$, the nonlinear natural frequencies of the system of the LFB and HFB, respectively, can be calculated as follows:

$$f_1 = \frac{1}{2\pi}\sqrt{\frac{k_1 + \alpha_1}{m_1}}, \quad f_2 = \frac{1}{2\pi}\sqrt{\frac{k_2 - \alpha_1}{m_2}}. \tag{16}$$

where the term α_1 is the coefficient of the linear term after expansion of the magnetic force with Taylor's series and is given by:

$$\alpha_1 = \frac{F_R(d^2 - 4Y_s^2)}{(d^2 + Y_s^2)^{7/2}} \tag{17}$$

Using Equation (16), the variation in the natural frequencies of the LFB and HFB with the separation distance between the two magnets is extracted and shown in Figure 5a,b, respectively. Additionally, the experimental variation in the natural frequencies with separation distance was recorded at a 0.1 g excitation level and reported for the LFB, as shown in Figure 5a. In contrast, the experimental natural frequency range of the HFB was hard to obtain due to the very small change in its natural frequency while changing the separation distance between the two magnets. Nevertheless, the LFB's experimental and simulated results show good agreement. Both plots of the LFB and HFB show a threshold separation distance of 15 mm, which matches the same value extracted from the static results shown in Figure 4. Additionally, Figure 5 shows that at a large separation distance, the magnetic force becomes weak, and the natural frequencies match the linear values of both beams. Lowering the separation distance toward the threshold, the natural frequency of the LFB drops to reach a minimum value of 12 Hz, and the natural frequency of the HFB reaches its maximum value of 263.2 Hz. Decreasing the separation distance more to the bistable range will increase the natural frequency of the LFB to a maximum value of 43 Hz and drop the natural frequency of the HFB to a minimum value of 261.4 Hz. This change in the natural frequencies of the LFB and HFB is because of the contribution of the magnetic force term (α_1) in Equation (17) that changes its sign according to the

value of d, which results in lowering or increasing the beams' natural frequencies. It is also noted that the natural frequency variation in the LFB is much more significant than that in the HFB due to the LFB's low-stiffness material (polymer) compared to the HFB's high-stiffness material (aluminum). It is obvious that the simulated data are not in perfect accordance with the experimental data in Figure 5a. Certainly, there are some discrepancies between the experimental and simulated data, which could be from the theoretical lumped-parameter model, which assumes the distributed mass of the beam to be lumped at one point. Moreover, the lack of accuracy in the magnetic force function used in the theoretical model could be another reason for the discrepancies between the theoretical and experimental results.

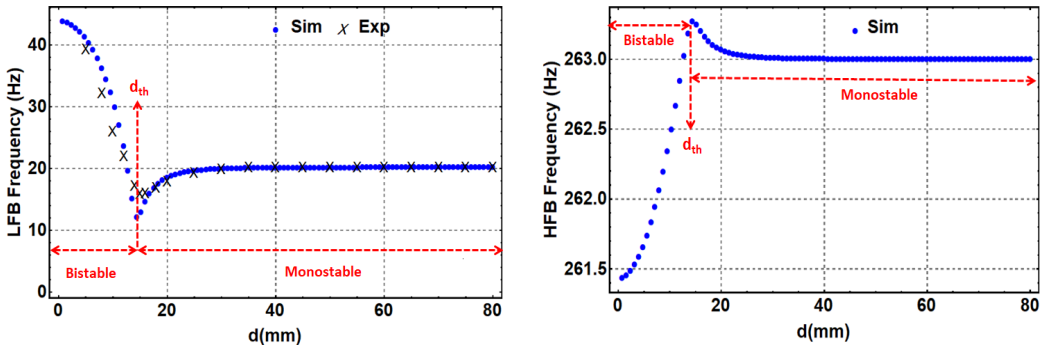

(**a**) (**b**)

Figure 5. (**a**) The simulated and experimental variations in the LFB's natural frequency with the separation distance. (**b**) The simulated variation in the HFB's natural frequency with the separation distance.

5.2.2. Linear Analysis

The linear response of the system and the generated voltage can be investigated by eliminating the effect of the magnetic force ($F_{magy} = 0$). Figure 6 summarizes the simulated and experimental frequency response curves of the LFB and HFB, and the frequency–voltage curve at a low excitation level of 0.05 g; all theoretical and experimental results are in good agreement. Figure 6a shows the LFB's theoretical and experimental frequency response curves, where the natural frequency is 20.8 Hz with a maximum deflection of 2.75 mm. Similarly, Figure 6b shows the simulated and experimental frequency response curves for the HFB with a natural frequency of 263 Hz and 0.0055 mm maximum deflection. Additionally, Figure 6c represents the frequency–voltage curve generated from the piezoelectric layer, where the voltage peaks approximately at 263 Hz with 5.9 mV as a maximum generated voltage. The maximum voltage is expected to be at the resonance of the beam (263 Hz) because the piezoelectric strip is attached to the HFB, so when the HFB reaches the resonance, the maximum deflection will occur, which means higher stresses and strains on the piezoelectric strip.

It is noticed that there are slight differences between the theoretical and experimental linear results. The reasons for such differences can be explained due to the deflection measurements. Theoretically, the tip magnets are assumed to be lumped with the cantilever beam's mass, but experimentally, this is not the case exactly. Additionally, some of the differences could be from the lumped-parameter modeling in the theoretical analysis, which does not consider the rotations of the tip magnets, which slightly affect the experimental measurements. Another reason for such differences could be related to the difference in perfection between the theory and experimental implementation. In the theoretical model, we assumed both beams to be fully clamped-free, whereas in the experiment, such a boundary was not ideally clamped. However, the lumped-parameter modeling shows a strong capability to predict the response accurately.

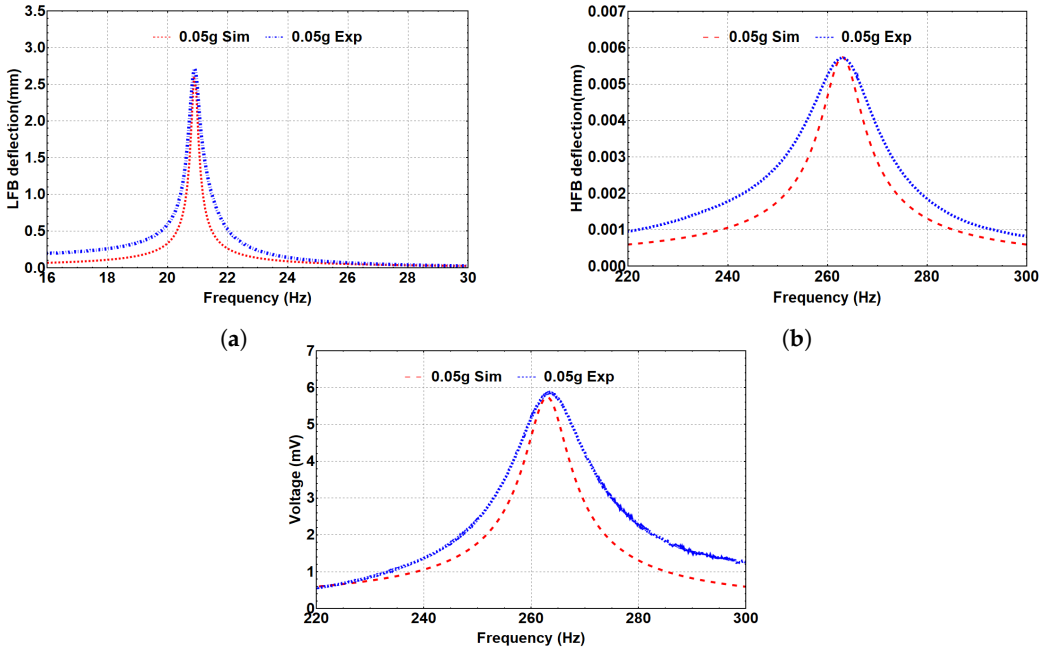

Figure 6. (**a**) Frequency response curve of the LFB. (**b**) Frequency response curve of the HFB. (**c**) Frequency–voltage curve of the HFB. The excitation level is 0.05 g.

5.2.3. Nonlinear Analysis

The system's dynamics were investigated at the three regimes: monostable, bistable, and threshold, with corresponding separation distances of 35 mm, 8 and 5 mm, and 15 mm, respectively. The generated frequency–voltage curves were extracted at the three regimes to show the frequency up-converter concept, where the voltage was generated at the LFB frequency range while the piezoelectric layer is attached to the HFB due to the magnetic coupling effect. At the monostable range, the separation distance was set to 35 mm, and the system was excited at different excitation levels, as shown in Figure 7a. Even though the piezoelectric strip was attached to the HFB, the voltage signal was generated at the LFB frequency range, proving the concept of the frequency up-conversion. Additionally, it is noted that higher output voltage was generated at higher excitation levels. Furthermore, nonlinear hardening behavior is shown with increasing the excitation level. Figure 7b shows that the simulated results agree with the experimental results at selected excitation levels of 0.1 and 0.5 g, which validates our theoretical model.

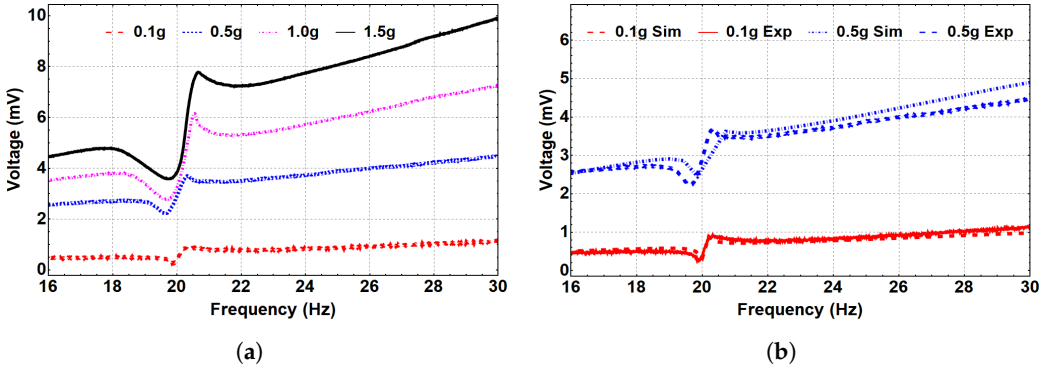

Figure 7. The frequency–voltage curve for different excitation levels at the monostable regime (d = 35 mm). (**a**) Experimental results. (**b**) Simulated results with experimental validation.

Next, we investigated the system's dynamic behavior in the bistable range. Toward this end, the system was subjected to different excitation levels at an 8 mm separation distance, as represented in Figure 8. As a result, a hardening behavior is shown where

the natural frequency is shifted to reach 30 Hz at the 0.1 g excitation level, compared to 20.8 Hz for the linear harvester. This shift in the natural frequency occurs because of the change in the distance between the two magnets in the coefficient α_1 of the magnetic force. With a further increase in the excitation level, the quadratic nonlinearity became dominant, and the natural frequency shifted to the left, indicating a softening behavior, as shown in Figure 8a. Moreover, the generated voltage in the bistable range significantly increased to reach 52 mV, compared to 6 mV for the monostable range at a 1.0 g excitation level. Figure 8b shows the simulated results and the experimental validation is in good agreement for various excitation levels.

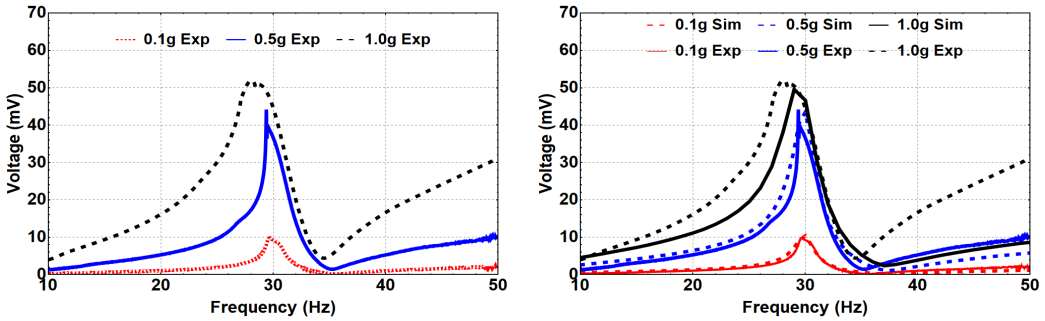

(**a**) (**b**)

Figure 8. The frequency–voltage curve for different excitation levels at the bistable regime ($d = 8$ mm). (**a**) Experimental results. (**b**) Simulated results with experimental validation.

Then, a separation distance of 5 mm was selected to investigate further the system's dynamic behavior in the bistable regime. Therefore, the system was subjected to different excitation levels, as shown in Figure 9. At 0.1 g, the natural frequency increased to 37.2 Hz, as shown in Figure 9a, compared to 20.8 Hz for the linear harvester, indicating a hardening behavior. This increment was due to the change in the distance between the two magnets in the coefficient α_1 of the magnetic force at low excitation levels, as reported previously. The natural frequency significantly increased at this separation distance compared to $d = 8$ mm at the same excitation level. This could be related to the higher magnetic coupling between the two beams at a smaller separation distance. When the excitation level increased, a softening behavior was noticed, which was more significant than the previous case at $d = 8$ mm. Additionally, the generated voltage significantly increased to around 170 mV at 1.5 g. The match between the experimental and simulated generated voltage at 0.1 and 0.5 g is presented in Figure 9b, and it shows good agreement that validates the theoretical model.

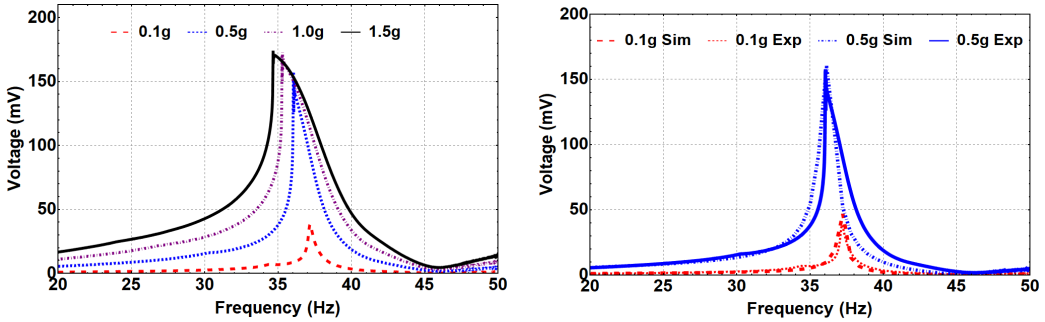

(**a**) (**b**)

Figure 9. The frequency–voltage curve for different excitation levels at the bistable regime ($d = 5$ mm). (**a**) Experimental results. (**b**) Simulated results with experimental validation.

Figure 10 shows the experimental and simulated generated voltage at the threshold regime where $d_{th} = 15$ mm. The system response of this region was investigated at different excitation levels. At 0.1 g, the natural frequency dropped to 17 Hz, reflecting a softening behavior, compared to 20.8 Hz for the linear harvester because of the separation distance

effect in the coefficient α_1 of the magnetic force, so the natural frequency decreases, as shown in Figure 10a. Additionally, by increasing the excitation level, the natural frequency starts to increase after 0.5 g, so a nonlinear hardening behavior is shown, indicating an interesting nonlinear combined behavior of softening and hardening. The nonlinear combined softening and hardening behavior can be related to the exchange in the dominance of the quadratic nonlinearity at low excitation levels to the cubic nonlinearity at higher excitation levels. Figure 10b shows the simulated generated voltage at different excitation levels for the same separation distance. Qualitatively, the simulated results show that the natural frequency dropped to reach a lower value than the linear harvester indicating softening behavior, whereas increasing the excitation level shows a hardening behavior which is different from the behavior of the experimental results shown in Figure 10a. This difference is because the model does not accurately match the experimental results in capturing the natural frequency at the threshold, as shown in Figure 5a, where the experimental natural frequency at $d_{th} = 15$ mm is approximately 17 Hz, whereas it is around 12 Hz for the simulated natural frequency. However, it is observed that the frequency–voltage curves show some mismatch between the simulation and the experiment, which seems to increase as the excitation level increases. This mismatch can be related to the high nonlinearity in the system at the threshold distance, where the system transfers between the monostable to the bistable range. Such behavior is not easily predicted accurately with the lumped-parameter model. However, these results are still considered qualitatively in good agreement. Furthermore, compared to the monostable region, the threshold plots show higher generated voltage for both simulation and experiment. At 0.1 g, the experimentally generated voltage was 1 mV in the monostable region, whereas it reached 2 mV at the threshold, which is 100% higher. Additionally, at the threshold with a 0.8 g excitation level, the experimentally measured voltage output peaked at almost 22 mV, compared to 8 mV at a higher excitation level of 1.5 g in the monostable region. This higher voltage generated at the threshold can be related to the higher coupling due to the lower separation distance than the monostable region.

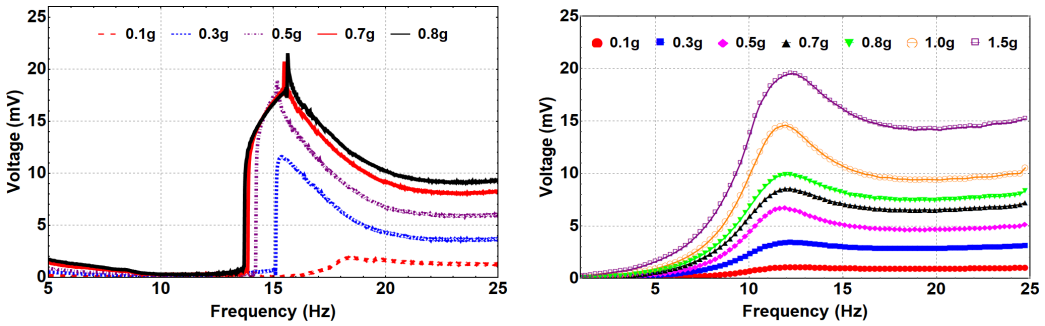

(**a**) (**b**)

Figure 10. The frequency–voltage curves for different excitation levels at the threshold regime ($d = 15$ mm). (**a**) Experimental results. (**b**) Simulated results.

The effect of the external resistance variation on the maximum output voltage has been investigated. Figure 11a shows the change in the maximum output voltage while changing the external resistance of the system within the bistable range at $d = 5$ mm at 0.5 g. The 200 kΩ was used in this study so far, and as shown in Figure 11a the maximum output voltage at this resistance value is approximately 0.16 V, and that was reported previously in Figure 9b. By decreasing the resistance to 100 kΩ, the produced voltage was reduced to roughly 0.09 V. When the resistance increased over 200 kΩ, the voltage also increased. At the resistance of 1 MΩ, the voltage went up to 0.7 V, then approximately doubled to reach 1.12 V at 2 MΩ. For the 25 MΩ, the produced voltage was 2.0 V. With a further resistance increase, the voltage no longer increased. Therefore, the maximum output voltage could be obtained at resistance of 25 MΩ. Moreover, the output power was calculated at different resistance values, as shown in Figure 11b. It is demonstrated that

the power increases by increasing the resistance until it is maximized at $R = 2$ MΩ with a value of approximately 0.76 μW, and any further increment in the resistance resulted in decreasing the output power, which dropped to approximately 0.185 μW and 0.15 μW for resistance levels of 25 and 50 MΩ, respectively. This observation concludes that 2 MΩ is the optimal resistance with maximum power. Therefore, it is worth mentioning that for maximizing the output power in practical applications, the optimum resistance that matches the internal impedance of the energy harvester needs to be investigated and used as the external resistance.

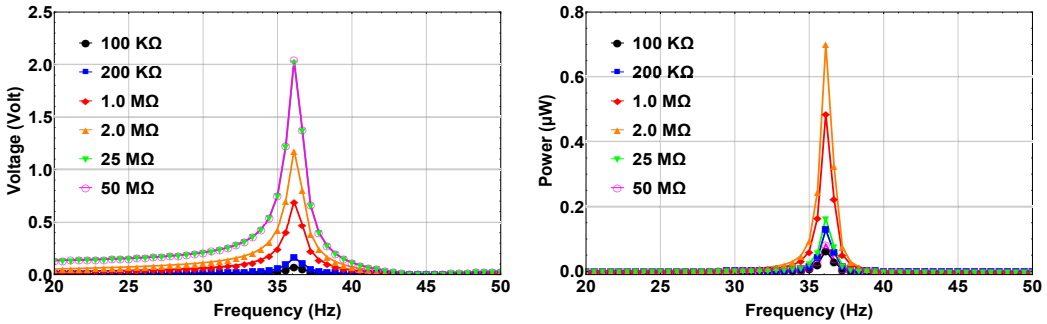

(**a**) (**b**)

Figure 11. (**a**) Maximum output voltage. (**b**) Maximum output power at different resistance values for a separation distance of 5 mm and an excitation level of 0.5 g.

In addition, the variations in output voltage and power with separation distance at different excitation levels are shown in Figure 12. We observed that both voltage and power increase when decreasing the distance between the two magnets from the monostable range toward the bistable range, and they are both maximized at the bistable region at $d = 5$ mm. These results reflect the influences of magnet spacing on the output voltage and power. The magnetic force is magnified and the energy is maximized in the bistable range compared to the monostable and threshold ranges.

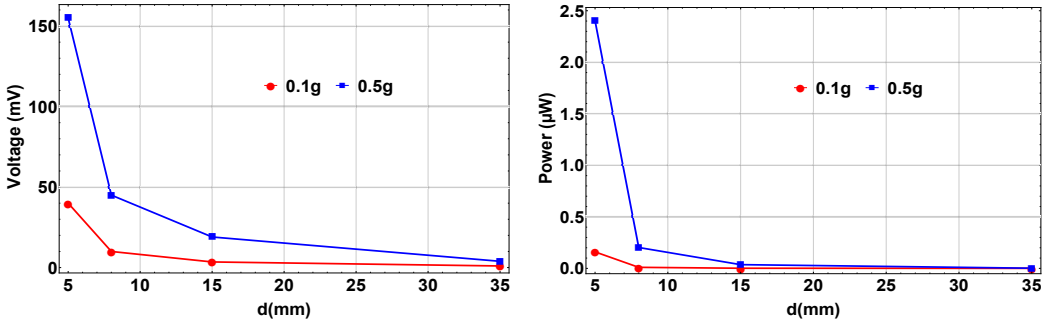

(**a**) (**b**)

Figure 12. (**a**) The variation in the output voltage with separation distance at different excitation levels. (**b**) The variation in the output power with separation distance at different excitation levels.

6. Conclusions

In conclusion, a frequency-up-converter piezoelectric energy harvester for low-vibration applications was investigated. The structure consists of two cantilever beams, a low-frequency beam (LFB), and a unimorph high-frequency beam (HFB) with an attached piezoelectric strip, and both beams are subjected to repulsive magnetic force from tip magnets. The structure was modeled as a two-degrees-of-freedom (2DOF) lumped-parameter model to study the static and dynamic behavior of the system. The static analysis resulted in a critical threshold separation distance of 15 mm that divides the system into monostable and bistable regions. The magnetic force transferred the vibrations and the harvested energy from a low-frequency range to a high-frequency range, which validated the concept of the frequency up-converter in energy harvesting applications. The linear response of

the system without magnetic effect elevated natural frequencies of 20.8 Hz for the LFB and 263 Hz for the HFB. In the monostable region, a nonlinear hardening behavior was captured. In contrast, a combination of softening and hardening behaviors were reported at the threshold. In the bistable region, the softening behavior was dominant. The amount of voltage signal generated was maximized in the bistable region with a 1000% increment at $d = 8$ mm and 4000% increment at $d = 5$ mm compared to the monostable region at the 0.1g excitation level. Additionally, the generated power peaked at 2 MΩ, which indicated that this value represents the optimal resistance. Therefore, magnetic nonlinearity can be utilized for frequency up-converting to enhance the efficiency of low-frequency external-vibration energy harvesters.

Author Contributions: M.A. performed the measurements, A.I. planned and supervised the work, M.A. and A.I. processed the experimental data, performed the analysis, drafted the manuscript, and designed the figures. A.R. aided in interpreting the results and worked on the manuscript. All authors discussed the results and commented on the manuscript. All authors have read and agreed to the published version of the manuscript.

Funding: This research received no external funding.

Informed Consent Statement: Not applicable.

Data Availability Statement: Data available on request from the authors.

Conflicts of Interest: The authors declare no conflict of interest.

Appendix A. The Coefficients of the Expanded Magnetic Force

$$
\begin{aligned}
\alpha_1 &= \frac{F_R(d^2 - 4Y_s^2)}{(d^2 + Y_s^2)^{7/2}} \\
\alpha_2 &= \frac{5F_R Y_s(-3d^2 + 4Y_s^2)}{2(d^2 + Y_s^2)^{9/2}} \\
\alpha_3 &= \frac{5F_R(d^4 - 12d^2Y_s^2 + 8Y_s^4)}{2(d^2 + Y_s^2)^{11/2}} \\
\alpha_4 &= \frac{35F_R Y_s(5d^4 - 20d^2Y_s^2 + 8Y_s^4)}{8(d^2 + Y_s^2)^{13/2}} \\
\alpha_5 &= \frac{7F_R(5d^6 - 120d^4Y_s^2 + 240d^2Y_s^4 - 64Y_s^6)}{8(d^2 + Y_s^2)^{15/2}} \\
\alpha_6 &= \frac{21F_R Y_S(-35d^6 + 280d^4Y_s^2 - 336d^2Y_s^4 + 64Y_s^6)}{16(d^2 + Y_s^2)^{17/2}} \\
\alpha_7 &= \frac{15F_R(7d^8 - 280d^6Y_s^2 + 1120d^4Y_s^4 - 896d^2Y_s^6 + 128Y_s^8)}{16(d^2 + Y_s^2)^{19/2}} \\
\alpha_8 &= \frac{165F_R Y_s(63d^8 - 840d^6Y_s^2 + 2016d^4Y_s^4 - 1152d^2Y_s^6 + 128Y_s^8)}{128(d^2 + Y_s^2)^{21/2}} \\
\alpha_9 &= \frac{55F_R(-21d^{10} + 1260d^8Y_s^2 - 8400d^6Y_s^4 + 13440d^4Y_s^6 - 5760d^2Y_s^8 + 512Y_s^{10})}{128(d^2 + Y_s^2)^{23/2}}
\end{aligned}
\tag{A1}
$$

References

1. Sullivan, J.; Gaines, L. *A Review of Battery Life-Cycle Analysis: State of Knowledge and Critical Needs*; Argonne National Lab. (ANL): Argonne, IL, USA, 2010.
2. Roundy, S.; Wright, P.; Rabaey, J. A study of low level vibrations as a power source for wireless sensor nodes. *Comput. Commun.* **2003**, *26*, 1131–1144. [CrossRef]
3. Miller, L.; Halvorsen, E.; Dong, T.; Wright, P. Modeling and experimental verification of low-frequency MEMS energy harvesting from ambient vibrations. *J. Micromechanics Microengineering* **2011**, *21*, 045029. [CrossRef]

4. Paci, D.; Schipani, M.; Bottarel, V.; Miatton, D. Optimization of a piezoelectric energy harvester for environmental broadband vibrations. In Proceedings of the 2008 15th IEEE International Conference On Electronics, Circuits Additionally, Systems, Saint Julian's, Malta, 31 August–3 September 2008; pp. 177–181.
5. Ibrahim, A.; Towfighian, S.; Younis, M.; Su, Q. Magnetoelastic beam with extended polymer for low frequency vibration energy harvesting. In Proceedings of the SPIE Smart Structures Additionally, Materials+ Nondestructive Evaluation Additionally, Health Monitoring, Las Vegas, NV, USA, 20–24 March 2016; p. 98060B.
6. McNutt, S. Observations and analysis of B-type earthquakes, explosions, and volcanic tremor at Pavlof Volcano, Alaska. *Bull. Seismol. Soc. Am.* **1986**, *76*, 153–175.
7. Reilly, E.; Miller, L.; Fain, R.; Wright, P. A study of ambient vibrations for piezoelectric energy conversion. *Proc. PowerMEMS* **2009**, *2009*, 312–315.
8. Tan, Y.; Dong, Y.; Wang, X. Review of MEMS electromagnetic vibration energy harvester. *J. Microelectromech. Syst.* **2016**, *26*, 1–16. [CrossRef]
9. Zhao, C.; Yang, Y.; Upadrashta, D.; Zhao, L. Design, modeling and experimental validation of a low-frequency cantilever triboelectric energy harvester. *Energy* **2021**, *214*, 118885. [CrossRef]
10. Ibrahim, A.; Ramini, A.; Towfighian, S. Triboelectric energy harvester with large bandwidth under harmonic and random excitations. *Energy Rep.* **2020**, *6*, 2490–2502. [CrossRef]
11. Kim, H.; Kim, J.; Kim, J. A review of piezoelectric energy harvesting based on vibration. *Int. J. Precis. Eng. Manuf.* **2011**, *12*, 1129–1141. [CrossRef]
12. Amin Karami, M.; Inman, D. Powering pacemakers from heartbeat vibrations using linear and nonlinear energy harvesters. *Appl. Phys. Lett.* **2012**, *100*, 042901. [CrossRef]
13. Qi, Y.; Jafferis, N.; Lyons Jr, K.; Lee, C.; Ahmad, H.; McAlpine, M. Piezoelectric ribbons printed onto rubber for flexible energy conversion. *Nano Lett.* **2010**, *10*, 524–528. [CrossRef]
14. Ali, S.; Friswell, M.; Adhikari, S. Analysis of energy harvesters for highway bridges. *J. Intell. Mater. Syst. Struct.* **2011**, *22*, 1929–1938. [CrossRef]
15. Erturk, A. Piezoelectric energy harvesting for civil infrastructure system applications: Moving loads and surface strain fluctuations. *J. Intell. Mater. Syst. Struct.* **2011**, *22*, 1959–1973. [CrossRef]
16. Anton, S.; Erturk, A.; Inman, D. Multifunctional unmanned aerial vehicle wing spar for low-power generation and storage. *J. Aircr.* **2012**, *49*, 292–301. [CrossRef]
17. Erturk, A.; Renno, J.; Inman, D. Modeling of piezoelectric energy harvesting from an L-shaped beam-mass structure with an application to UAVs. *J. Intell. Mater. Syst. Struct.* **2009**, *20*, 529–544. [CrossRef]
18. Featherston, C.; Holford, K.; Greaves, B. Harvesting vibration energy for structural health monitoring in aircraft. *Key Eng. Mater.* **2009**, *413*, 439–446. [CrossRef]
19. Lee, S.; Youn, B. A new piezoelectric energy harvesting design concept: Multimodal energy harvesting skin. *IEEE Trans. Ultrason. Ferroelectr. Freq. Control.* **2011**, *58*, 629–645. [CrossRef]
20. Le, M.; Capsal, J.; Lallart, M.; Hebrard, Y.; Van Der Ham, A.; Reffe, N.; Geynet, L.; Cottinet, P. Review on energy harvesting for structural health monitoring in aeronautical applications. *Prog. Aerosp. Sci.* **2015**, *79*, 147–157. [CrossRef]
21. Mann, B.; Sims, N. Energy harvesting from the nonlinear oscillations of magnetic levitation. *J. Sound Vib.* **2009**, *319*, 515–530. [CrossRef]
22. Erturk, A.; Inman, D. Broadband piezoelectric power generation on high-energy orbits of the bistable Duffing oscillator with electromechanical coupling. *J. Sound Vib.* **2011**, *330*, 2339–2353. [CrossRef]
23. Triplett, A.; Quinn, D. The effect of non-linear piezoelectric coupling on vibration-based energy harvesting. *J. Intell. Mater. Syst. Struct.* **2009**, *20*, 1959–1967. [CrossRef]
24. Stanton, S.; Erturk, A.; Mann, B.; Inman, D. Nonlinear piezoelectricity in electroelastic energy harvesters: Modeling and experimental identification. *J. Appl. Phys.* **2010**, *108*, 074903. [CrossRef]
25. Kim, P.; Bae, S.; Seok, J. Resonant behaviors of a nonlinear cantilever beam with tip mass subject to an axial force and electrostatic excitation. *Int. J. Mech. Sci.* **2012**, *64*, 232–257. [CrossRef]
26. Abdelkefi, A.; Nayfeh, A.; Hajj, M. Global nonlinear distributed-parameter model of parametrically excited piezoelectric energy harvesters. *Nonlinear Dyn.* **2012**, *67*, 1147–1160. [CrossRef]
27. Kim, P.; Yoon, Y.; Seok, J. Nonlinear dynamic analyses on a magnetopiezoelastic energy harvester with reversible hysteresis. *Nonlinear Dyn.* **2016**, *83*, 1823–1854. [CrossRef]
28. Dos Santos, M.; Ferreira, J.; Simões, J.; Pascoal, R.; Torrão, J.; Xue, X.; Furlani, E. Magnetic levitation-based electromagnetic energy harvesting: A semi-analytical non-linear model for energy transduction. *Sci. Rep.* **2016**, *6*, 18579. [CrossRef]
29. Seol, M.; Han, J.; Jeon, S.; Meyyappan, M.; Choi, Y. Floating oscillator-embedded triboelectric generator for versatile mechanical energy harvesting. *Sci. Rep.* **2015**, *5*, 16409. [CrossRef]
30. Ibrahim, A.; Towfighian, S.; Younis, M. Dynamics of transition regime in bistable vibration energy harvesters. *J. Vib. Acoust.* **2017**, *139*, 051008. [CrossRef]
31. Covaci, C.; Gontean, A. Piezoelectric energy harvesting solutions: A review. *Sensors* **2020**, *20*, 3512. [CrossRef]
32. Izadgoshasb, I.; Lim, Y.; Tang, L.; Padilla, R.; Tang, Z.; Sedighi, M. Improving efficiency of piezoelectric based energy harvesting from human motions using double pendulum system. *Energy Convers. Manag.* **2019**, *184*, 559–570. [CrossRef]

33. Ibrahim, S.; Ali, W. A review on frequency tuning methods for piezoelectric energy harvesting systems. *J. Renew. Sustain. Energy* **2012**, *4*, 062703. [CrossRef]
34. Zhu, D.; Roberts, S.; Tudor, M.; Beeby, S. Design and experimental characterization of a tunable vibration-based electromagnetic micro-generator. *Sens. Actuators A Phys.* **2010**, *158*, 284–293. [CrossRef]
35. Sun, W.; Jung, J.; Wang, X.; Kim, P.; Seok, J.; Jang, D. Design, simulation, and optimization of a frequency-tunable vibration energy harvester that uses a magnetorheological elastomer. *Adv. Mech. Eng.* **2015**, *7*, 147421. [CrossRef]
36. Wickenheiser, A.; Garcia, E. Broadband vibration-based energy harvesting improvement through frequency up-conversion by magnetic excitation. *Smart Mater. Struct.* **2010**, *19*, 065020. [CrossRef]
37. Masana, R.; Daqaq, M. Electromechanical modeling and nonlinear analysis of axially loaded energy harvesters. *J. Vib. Acoust.* **2011**, *133*, 011007. [CrossRef]
38. Gammaitoni, L.; Neri, I.; Vocca, H. Nonlinear oscillators for vibration energy harvesting. *Appl. Phys. Lett.* **2009**, *94*, 164102. [CrossRef]
39. Soliman, M.; Abdel-Rahman, E.; El-Saadany, E.; Mansour, R. A design procedure for wideband micropower generators. *J. Microelectromech. Syst.* **2009**, *18*, 1288–1299. [CrossRef]
40. Moon, F.; Holmes, P. A magnetoelastic strange attractor. *J. Sound Vib.* **1979**, *65*, 275–296. [CrossRef]
41. Stanton, S.; Owens, B.; Mann, B. Harmonic balance analysis of the bistable piezoelectric inertial generator. *J. Sound Vib.* **2012**, *331*, 3617–3627. [CrossRef]
42. Gu, L.; Livermore, C. Impact-driven, frequency up-converting coupled vibration energy harvesting device for low frequency operation. *Smart Mater. Struct.* **2011**, *20*, 045004. [CrossRef]
43. Liu, H.; Lee, C.; Kobayashi, T.; Tay, C.; Quan, C. Piezoelectric MEMS-based wideband energy harvesting systems using a frequency-up-conversion cantilever stopper. *Sens. Actuators A Phys.* **2012**, *186*, 242–248. [CrossRef]
44. Zorlu, Ö.; Topal, E.; Külah, H. A vibration-based electromagnetic energy harvester using mechanical frequency up-conversion method. *IEEE Sens. J.* 2010, *11*, 481–488. [CrossRef]
45. Sari, I.; Balkan, T.; Külah, H. An electromagnetic micro power generator for low-frequency environmental vibrations based on the frequency upconversion technique. *J. Microelectromech. Syst.* **2009**, *19*, 14–27. [CrossRef]
46. Galchev, T.; Kim, H.; Najafi, K. Micro power generator for harvesting low-frequency and nonperiodic vibrations. *J. Microelectromech. Syst.* **2011**, *20*, 852–866. [CrossRef]
47. Ashraf, K.; Khir, M.; Dennis, J.; Baharudin, Z. A wideband, frequency up-converting bounded vibration energy harvester for a low-frequency environment. *Smart Mater. Struct.* **2013**, *22*, 025018. [CrossRef]
48. Fakeih, E. Harvesting Mechanical Vibrations Using a Frequency Up-Converter. Master's Thesis, KAUST Department, Thuwal, Saudi Arabia, 2020.
49. Fakeih, E.; Almansouri, A.; Kosel, J.; Younis, M.; Salama, K. A Wideband Magnetic Frequency Up-Converter Energy Harvester. *Adv. Eng. Mater.* **2021**, 23, 2001364. [CrossRef]
50. Atmeh, M.; Ibrahim, A. Modeling of Piezoelectric Vibration Energy Harvesting From Low-Frequency Using Frequency Up-Conversion. *Smart Mater. Adapt. Struct. Intell. Syst.* **2021**, *85499*, V001T04A011.
51. Edwards, B.; Xie, M.; Aw, K.; Hu, A.; Gao, W. An impact based frequency up-conversion mechanism for low frequency vibration energy harvesting. In Proceedings of the 2013 Transducers & Eurosensors XXVII: The 17th International Conference On Solid-State Sensors, Actuators Additionally, Microsystems (TRANSDUCERS & EUROSENSORS XXVII), Barcelona, Spain, 16–20 June 2013; pp. 1344–1347.
52. Liu, H.; Lee, C.; Kobayashi, T.; Tay, C.; Quan, C. Investigation of a MEMS piezoelectric energy harvester system with a frequency-widened-bandwidth mechanism introduced by mechanical stoppers. *Smart Mater. Struct.* **2012**, *21*, 035005. [CrossRef]
53. Pozzi, M.; Zhu, M. Plucked piezoelectric bimorphs for energy harvesting applications. *Smart Sens. Actuators MEMS V* **2011**, *8066*, 806616.
54. Moss, S.; Barry, A.; Powlesland, I.; Galea, S.; Carman, G. A low profile vibro-impacting energy harvester with symmetrical stops. *Appl. Phys. Lett.* **2010**, *97*, 234101. [CrossRef]
55. Halim, M.; Cho, H.; Park, J. Design and experiment of a human-limb driven, frequency up-converted electromagnetic energy harvester. *Energy Convers. Manag.* **2015**, *106*, 393–404. [CrossRef]
56. Fu, H.; Yeatman, E. A methodology for low-speed broadband rotational energy harvesting using piezoelectric transduction and frequency up-conversion. *Energy* **2017**, *125*, 152–161. [CrossRef]
57. Jung, S.; Yun, K. Energy-harvesting device with mechanical frequency-up conversion mechanism for increased power efficiency and wideband operation. *Appl. Phys. Lett.* **2010**, *96*, 111906. [CrossRef]
58. Kulah, H.; Najafi, K. Energy scavenging from low-frequency vibrations by using frequency up-conversion for wireless sensor applications. *IEEE Sens. J.* **2008**, *8*, 261–268. [CrossRef]
59. Almansouri, A.; Salama, K.; Kosel, J. Magneto-Acoustic Resonator for Aquatic Animal Tracking. *IEEE Trans. Magn.* **2018**, *55*, 1–4. [CrossRef]
60. Marinkovic, B.; Koser, H. Smart sand—a wide bandwidth vibration energy harvesting platform. *Appl. Phys. Lett.* **2009**, *94*, 103505. [CrossRef]
61. Tvedt, L.; Nguyen, D.; Halvorsen, E. Nonlinear behavior of an electrostatic energy harvester under wide-and narrowband excitation. *J. Microelectromech. Syst.* **2010**, *19*, 305–316. [CrossRef]

62. Miki, D.; Honzumi, M.; Suzuki, Y.; Kasagi, N. Large-amplitude MEMS electret generator with nonlinear spring. In Proceedings of the 2010 IEEE 23rd International Conference On Micro Electro Mechanical Systems (MEMS), Hong Kong, China, 24–28 January 2010; pp. 176–179.
63. Erturk, A.; Hoffmann, J.; Inman, D. A piezomagnetoelastic structure for broadband vibration energy harvesting. *Appl. Phys. Lett.* **2009**, *94*, 254102. [CrossRef]
64. Cammarano, A.; Burrow, S.; Barton, D. Modelling and experimental characterization of an energy harvester with bi-stable compliance characteristics. *Proc. Inst. Mech. Eng. Part I J. Syst. Control. Eng.* **2011**, *225*, 475–484. [CrossRef]
65. Andò, B.; Baglio, S.; Trigona, C.; Dumas, N.; Latorre, L.; Nouet, P. Nonlinear mechanism in MEMS devices for energy harvesting applications. *J. Micromechanics Microengineering* **2010**, *20*, 125020. [CrossRef]
66. Ferrari, M.; Baù, M.; Guizzetti, M.; Ferrari, V. A single-magnet nonlinear piezoelectric converter for enhanced energy harvesting from random vibrations. *Sens. Actuators A Phys.* **2011**, *172*, 287–292. [CrossRef]
67. Ferrari, M.; Ferrari, V.; Guizzetti, M.; Ando, B.; Baglio, S.; Trigona, C. Improved energy harvesting from wideband vibrations by nonlinear piezoelectric converters. *Sens. Actuators A Phys.* **2010**, *162*, 425–431. [CrossRef]
68. Lin, J.; Lee, B.; Alphenaar, B. The magnetic coupling of a piezoelectric cantilever for enhanced energy harvesting efficiency. *Smart Mater. Struct.* **2010**, *19*, 045012. [CrossRef]
69. Al-Ashtari, W.; Hunstig, M.; Hemsel, T.; Sextro, W. Frequency tuning of piezoelectric energy harvesters by magnetic force. *Smart Mater. Struct.* **2012**, *21*, 035019. [CrossRef]
70. Tang, L.; Wu, H.; Yang, Y.; Soh, C. Optimal performance of nonlinear energy harvesters. In Proceedings of the 22nd International Conference On Adaptive Structures Additionally, Technologies (ICAST), Corfu, Greece 10–12 October 2011.
71. Tang, L.; Yang, Y.; Soh, C. Improving functionality of vibration energy harvesters using magnets. *J. Intell. Mater. Syst. Struct.* **2012**, *23*, 1433–1449. [CrossRef]
72. Noh, J.; Kim, P.; Yoon, Y. Load Resistance Optimization of a Magnetically Coupled Two-Degree-of-Freedom Bistable Energy Harvester Considering Third-Harmonic Distortion in Forced Oscillation. *Sensors* **2021**, *21*, 2668. [CrossRef] [PubMed]
73. Li, X.; Li, Z.; Huang, H.; Wu, Z.; Huang, Z.; Mao, H.; Cao, Y. Broadband spring-connected bi-stable piezoelectric vibration energy harvester with variable potential barrier. *Results Phys.* **2020**, *18*, 103173. [CrossRef]
74. Younis, M. *MEMS Linear and Nonlinear Statics and Dynamics*; Springer Science & Business Media: Berlin/Heidelberg, Germany, 2011.

Disclaimer/Publisher's Note: The statements, opinions and data contained in all publications are solely those of the individual author(s) and contributor(s) and not of MDPI and/or the editor(s). MDPI and/or the editor(s) disclaim responsibility for any injury to people or property resulting from any ideas, methods, instructions or products referred to in the content.